Determining hydrodynamic forces in bursting bubbles using DNA nanotube mechanics

Rizal F. Hariadi[1], Erik Winfree[2], and Bernard Yurke[3]

[1] *Applied Physics, California Institute of Technology, Pasadena, CA 91125, USA*
[2] *Bioengineering, California Institute of Technology, Pasadena, CA 91125, USA*
[3] *College of Engineering, Boise State University, Boise, ID 83725, USA*

Contents

1 Strand sequences

Name	Sequence
U1-TT-Cy3	5'- Cy3-TT-GGCGATTAGG-ACGCTAAGCCA-CCTTTAGATCC-TGTATCTGGT -3'
U2	5'- GGATCTAAAGG-ACCAGATACA-CCACTCTTCC-TGACATCTTGT -3'
U3	5'- GGAAGAGTGG-ACAAGATGTCA-CCGTGAGAACC-TGCAATGCGT -3'
U4	5'- GGTTCTCACGG-ACGCATTGCA-CCGCACGACC-TGTTCGACAGT -3'
U5	5'- GGTCGTGCGG-ACTGTCGAACA-CCAACGATGCC-TGATAGAAGT -3'
U6	5'- GGCATCGTTGG-ACTTCTATCA-ATGCACCTCC-AGCTTTGAATG -3'
T7 (modified)	5'- GGAGGTGCAT-CATTCAAAGCT-TGGCTTAGCGT-CCTAATCGCC -3'

Table S1: DNA sequences for 7-helix DNA nanotube. Apart from the oligomer T7, we have employed the published DNA sequences in ref. [1]. The modified T7 strand was designed to reduce the twist energy in the 7-helix nanotube (c.f. Ref. [2]) as shown in Fig. S1. A Cy3 fluorophore was attached to the U1 strand for fluorescent imaging

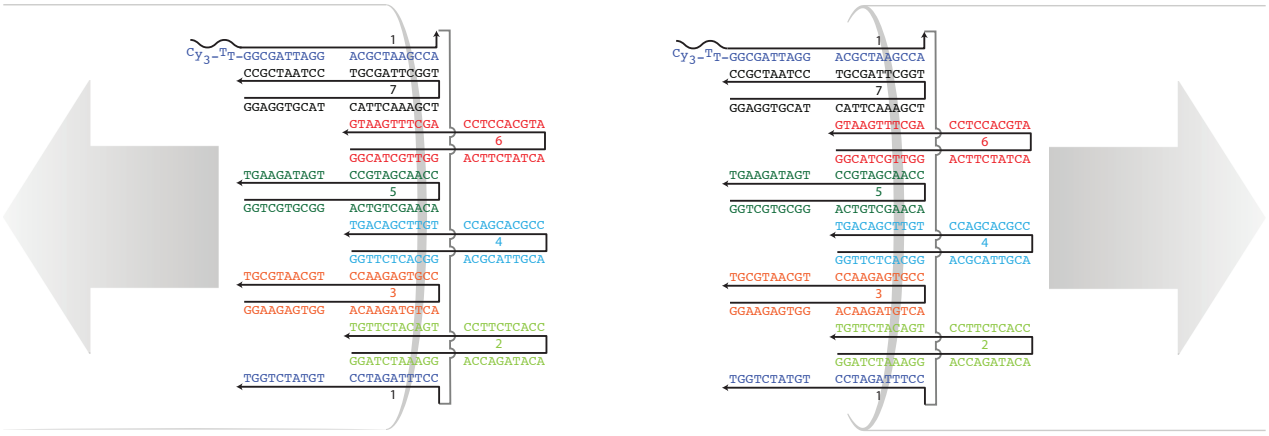

Figure S1: Strand diagram for 7-helix DNA nanotubes. Each strand has four sticky ends; each sticky end has a unique complement in its adjacent strand. The interactions between complementary sticky ends drives the nucleation and polymerization reactions to form the designed tubular structure.

2 Supplementary Histograms

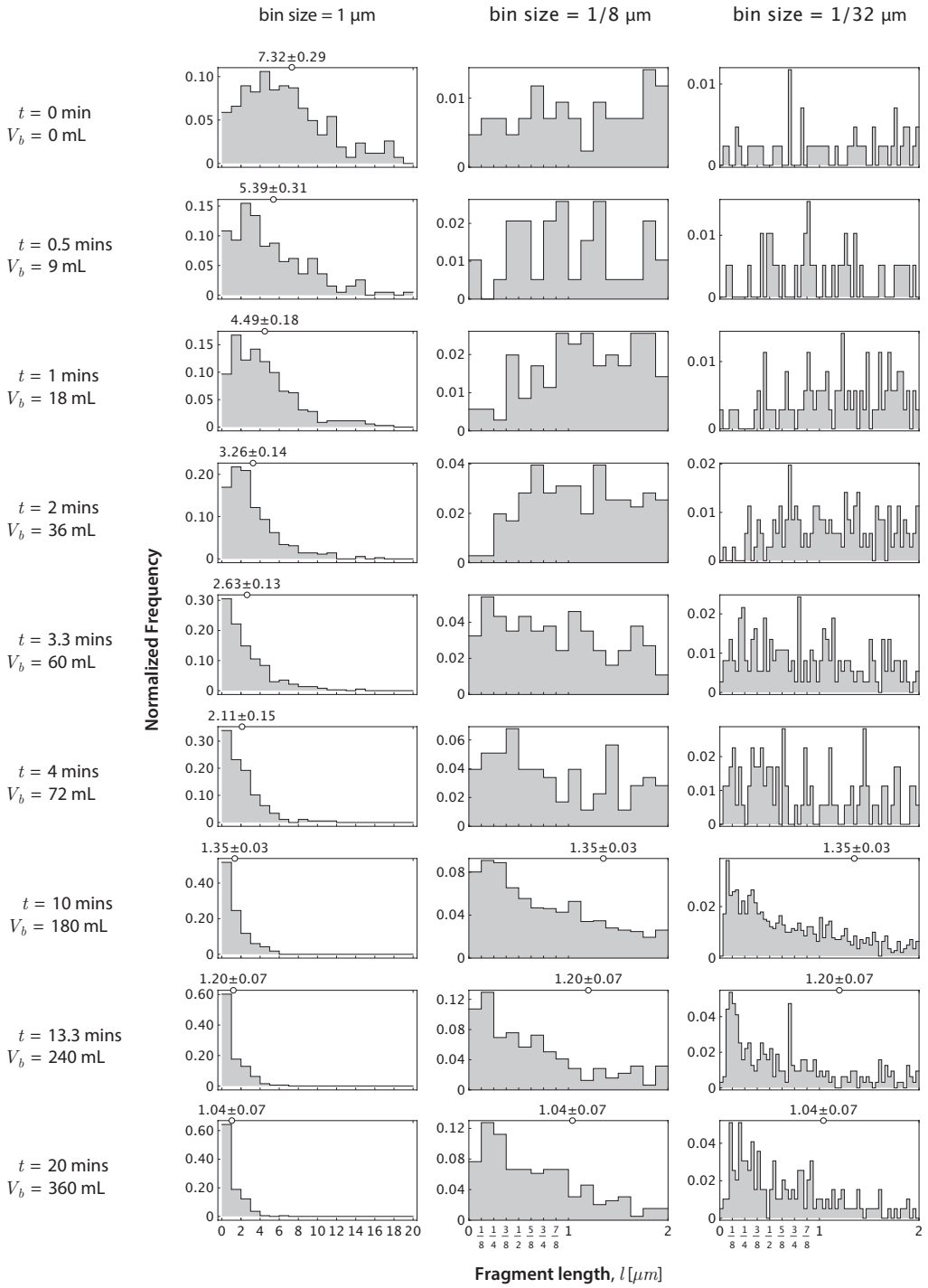

Figure S2: *Fragment length distribution for experiments in assay buffer at different exposure times with an 18 mL/min air flow rate.* The smallest bin in the histogram with bin size $= 1/32\ \mu m$ is relatively unaltered during the fragmentation experiments. The constant level of the $1/32\ \mu m$ bin was used to infer the maximum elongational flow rate during bubble bursting.

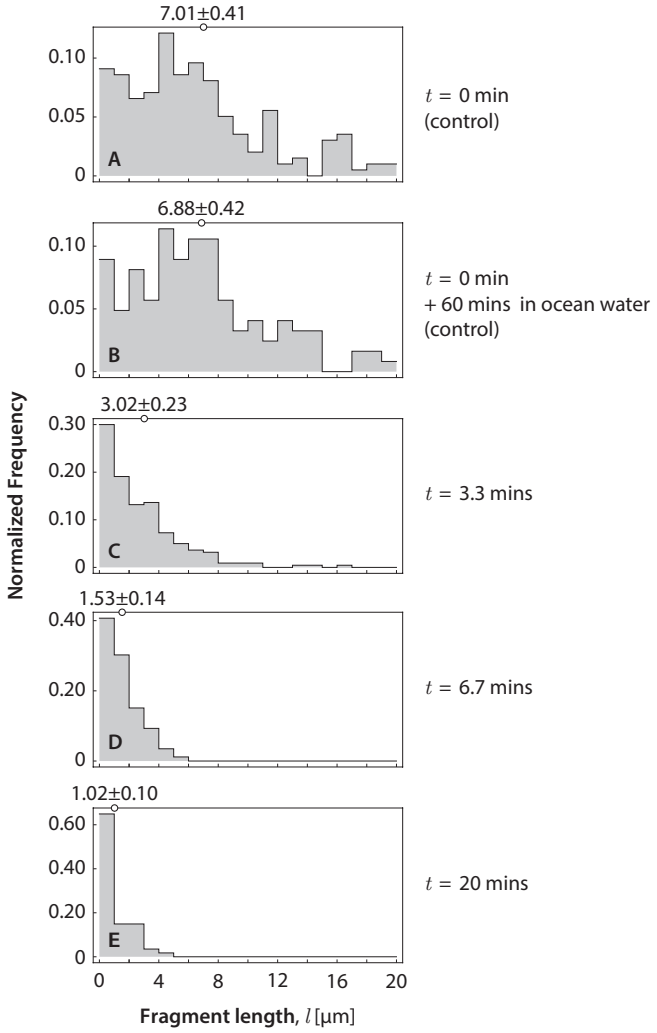

Figure S3: *Length distribution for the fragmentation experiments with ocean water.* (*A–B*) Length histograms of unperturbed DNA nanotubes in ocean water at t = 0 (*A*) and 1 hour (*B*). (*C–E*) Nanotube length distribution for the fragmentation experiments with ocean water at different air volume at 18 mL/min flow rate.

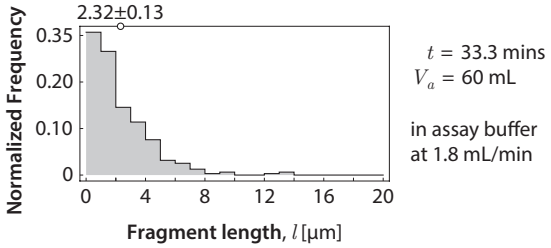

Figure S4: *The fluid flow associated with bubble inflation and formation is not responsible for fragmentation.* Fragment length distribution for the experiment with the slower flow rate (1.8 mL/min) for 33.3 min is similar to the corresponding bubble bursting experiment at 18 mL/min for 3.33 min (Fig. S2). In both cases, the total air volume was 60 mL. The $t = 0$ min length histogram in Fig. S2 provides a justifiable negative control for this experiment. Although the data in Figs. S2 and S4 were acquired on different days, the starting nanotube samples were prepared and annealed at the same time.

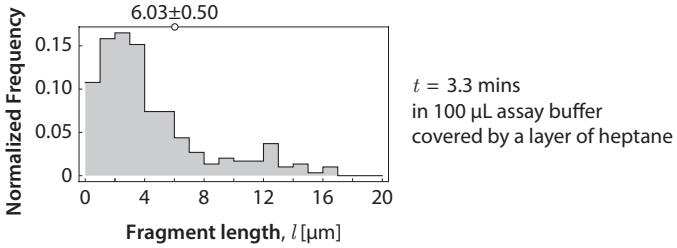

Figure S5: *Nanotube fragmentation is primarily due to the fluid flows associated with bubble bursting.* Fragment length histogram for the experiment in assay buffer under a layer of heptane at 18 mL/min flow rate for 3.3 mins. The length histogram is comparable to the initial nanotube length distribution (Fig. S2). The $t = 0$ min length histogram in Fig. S2 is used as control data because these experiments used the same DNA nanotube sample.

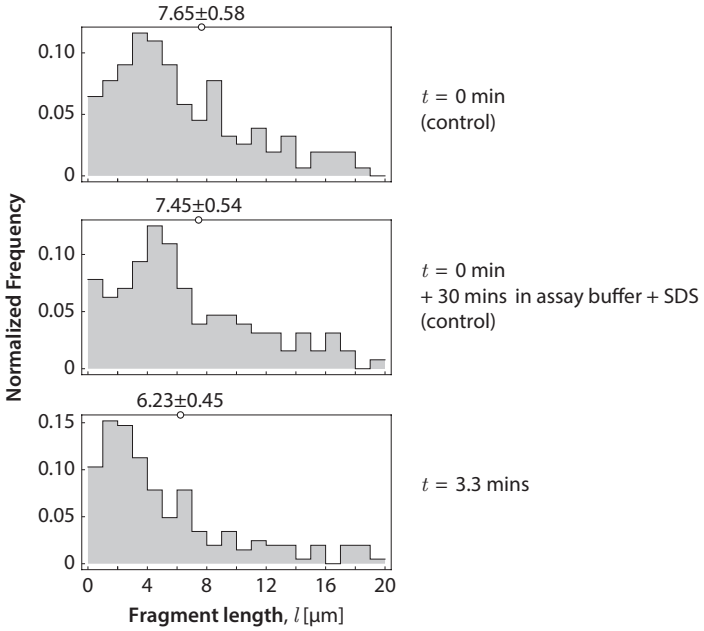

Figure S6: *Surface tension controls the maximum elongational rate in bubble bursting.* (*Upper–middle*) Similar length histograms before (*upper*) and after (*middle*) 30 mins incubation in 1% SDS showing the stability of DNA nanotubes in the SDS containing buffer. (*Lower*) Fragment length distribution for the control experiment in 1% SDS containing buffer. The change of length distribution is substantially less than the corresponding experiment in assay buffer (Fig. S2).

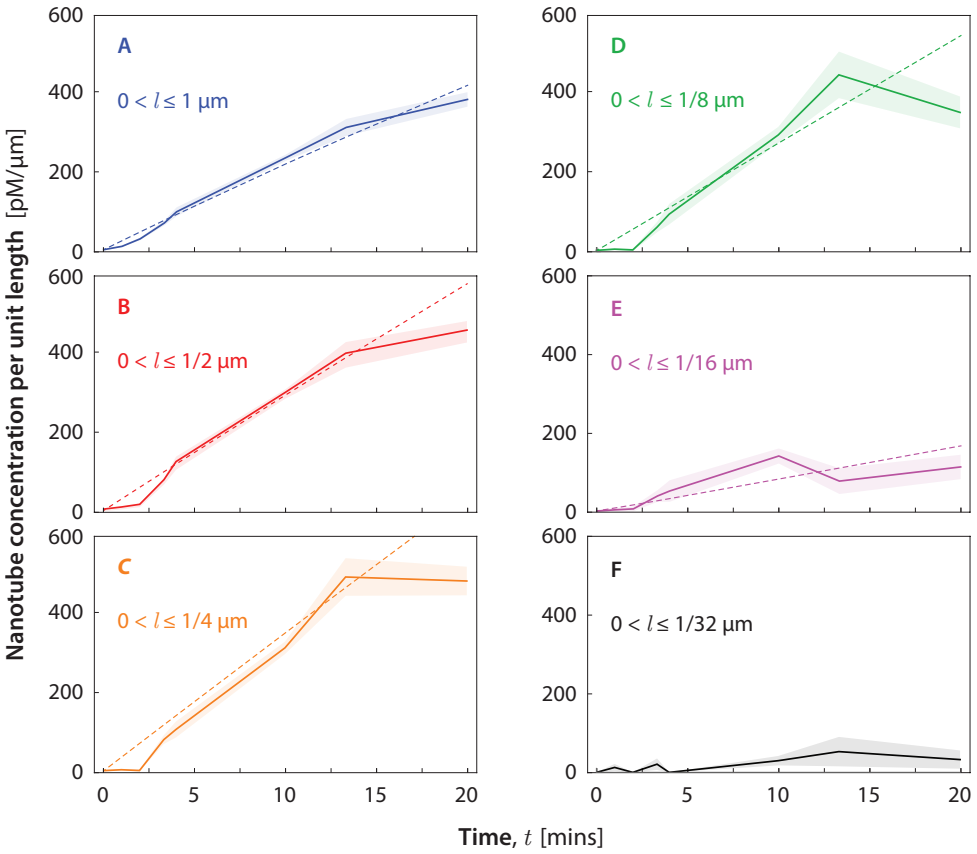

Figure S7: Experimental (solid line) and simulated (dashed, full cascade model) plots of histogram bin values for fragment lengths less than the indicated bin size over the course of the fragmentation experiment. The relative concentrations of nanotubes with $l > 1/16$ μm grow similarly with time (*A*–*D*). Those with $l < 1/16$ μm also grow, but less markedly (*E*). The number of nanotubes with $l < 1/32$ μm is essentially negligible over the course of the experiment (*F*). Shaded area indicates S.E.M. from bootstrapping.

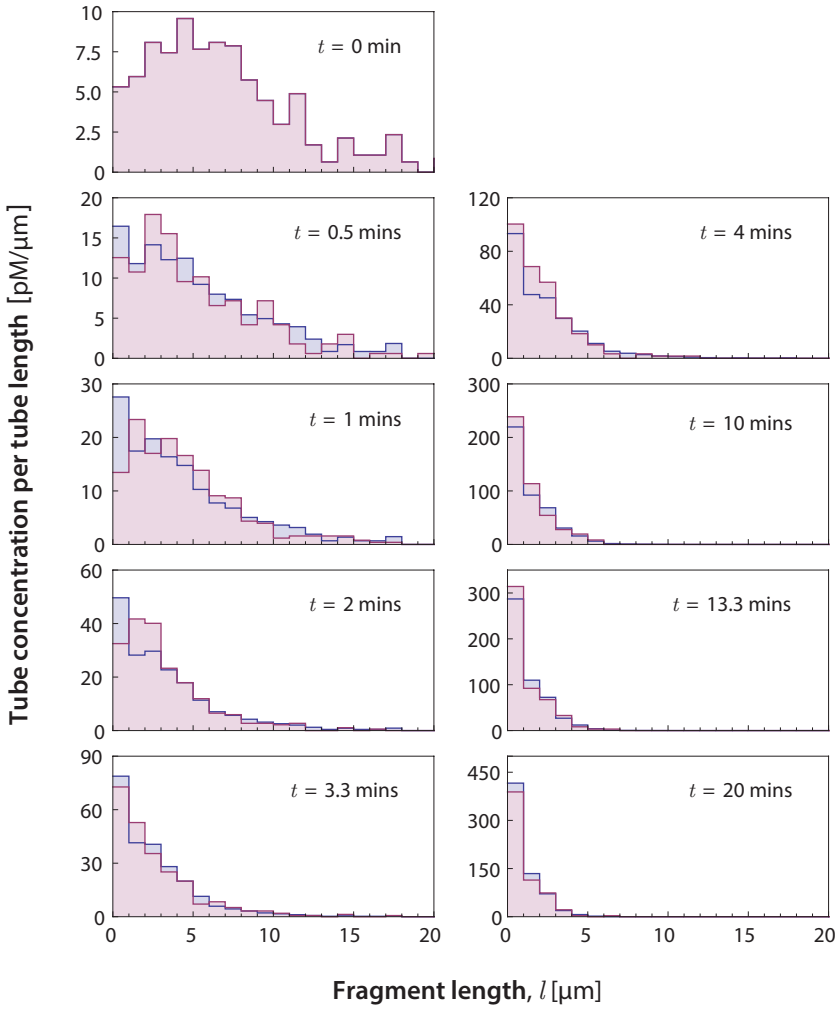

Figure S8: Simulated (blue) and experimental (red) fragment length distributions for the fragmentation experiment with assay buffer. The simulated length histogram is generated deterministically by the full cascade model (Eq. 8 of the main text and SI sections 3 and 4), where a nanotube of length l is broken into 2^n fragments based on its $V_f(l)$. This model fits our data better than the single bifurcation model in Fig. S9.

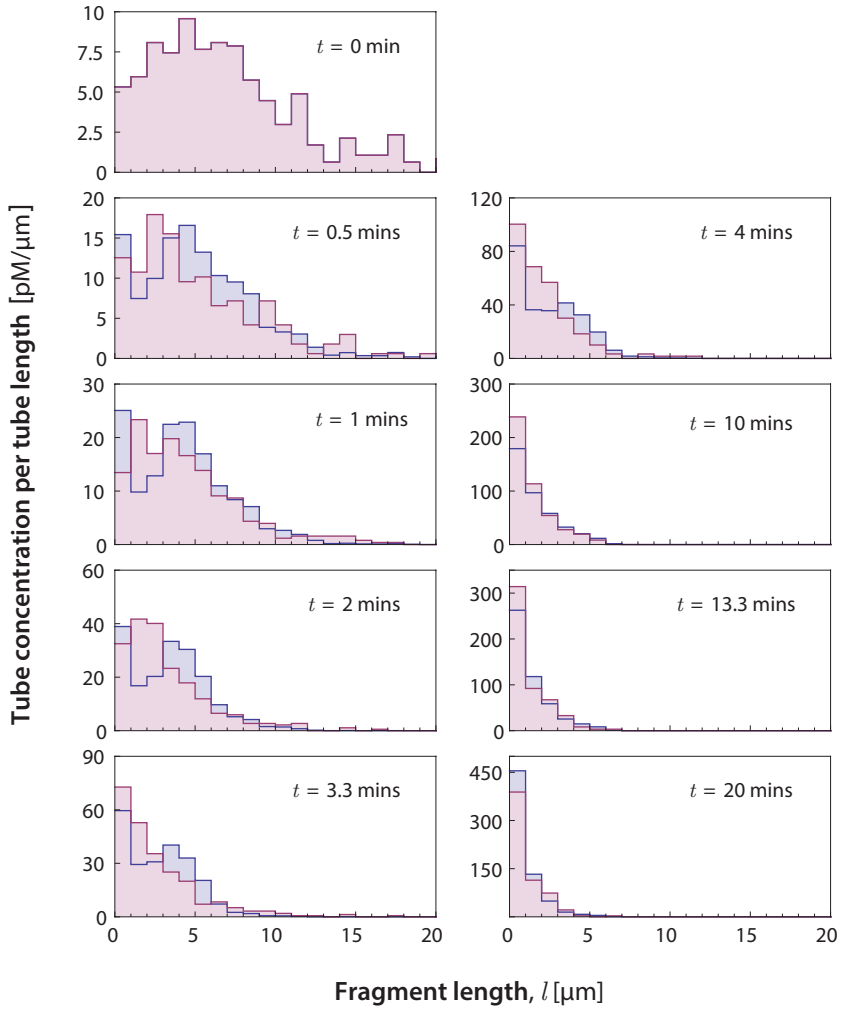

Figure S9: Simulated (blue) and experimental (red) fragment length distributions for the fragmentation experiment with assay buffer. The simulated fragment histograms are based on the single bifurcation model where nanotubes of length $2l_i$ are broken into exactly two fragments of length l_i (as described in Eq. 7 of the main text and section 5 of the SI). The value of the goodness of fit parameter, defined in Eq. (S64), is a factor of 4.1 worse than that for the full cascade model used in Fig. S8. The lower goodness of fit value is also reflected in the $c(l,t)$ distributions which exhibit a bulge, for short and intermediate times, that is absent in the experimental data.

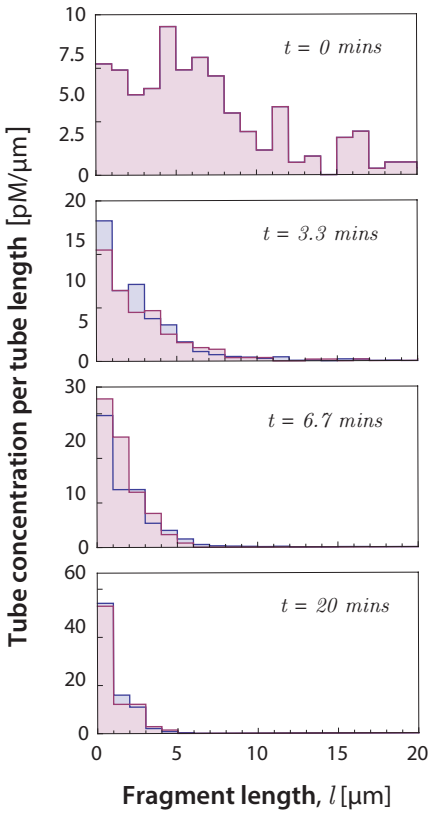

Figure S10: Simulated (blue) and experimental (red) nanotube length histogram for bubble bursting experiment in ocean water at t= 0, 3.3, 6.7, and 20 mins, using the full cascade model.

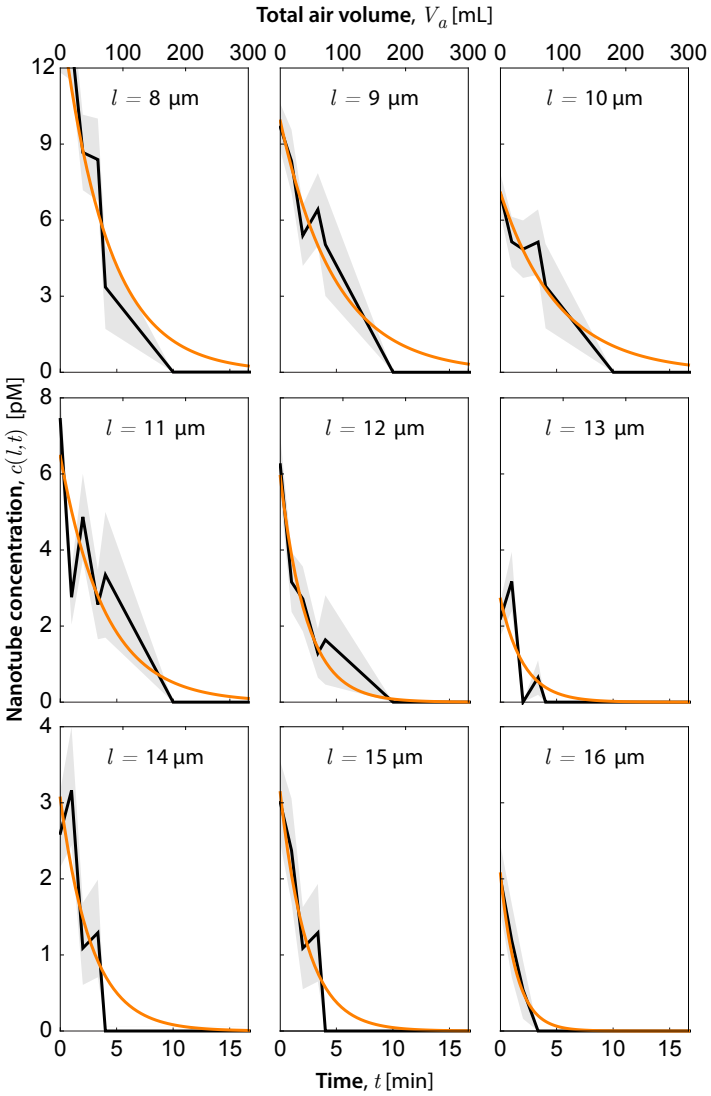

Figure S11: *Quantifying characteristic fragmentation volume $V_f(l)$ based on the evolution of nanotube concentrations.* The concentration for nanotubes in the indicated length interval ($l-1$ μm) to ($l+1$ μm) (black lines) at different time points ($t = V_a/\dot{V}_a$ with $\dot{V}_a = \gamma V_b$=18 mL/min, where γ is the bubble production rate and V_b is the measured bubble volume). Orange lines are single exponential fits of $c(l,t)$ to $\alpha e^{-\beta t}$ with characteristic decay constant $\beta = \gamma V_f(l)/V_s$, where V_s is the sample volume (100 μL). Error bars (gray-shaded regions) represent S.E.M. from bootstrapping.

3 Details for derivation of the full cascade model

Using Eqs. (4), (5), and (6) of the main text, and performing the l' integration, Eq. (2) yields

$$\frac{dc(l,t)}{dt} = -\frac{\gamma V_f(l)}{V_s} c(l,t) + \frac{\gamma}{V_s} \sum_{m=1}^{\infty} 2^{2m} p_m(2^m l) V_f(2^m l) c(2^m l, t). \tag{S1}$$

As a consistency check, again using Eqs. (4), (5), and (6), and performing the l' integration, Eq. (3) yields the condition

$$\sum_{m=1}^{\infty} p_m(l) = 1 \tag{S2}$$

which we know must hold, since $p_m(l)$ is the conditional probability that a tube of length l will fragment into 2^m tubes when it breaks.

A further simplification of the model is achieved as follows. From the definitions of the quantities on the right hand side,

$$\gamma_m(l) = \frac{\gamma}{V_s} p_m(l) V_f(l) \tag{S3}$$

is the rate that a tube of length l in the sample volume is broken into 2^m fragments and

$$\gamma_T(l) = \frac{\gamma V_f(l)}{V_s} \tag{S4}$$

is the rate that a tube of length l in the sample volume is broken. Hence, one must have

$$\gamma_T(l) = \sum_{k=1}^{\infty} \gamma_k(l). \tag{S5}$$

Since we are considering a cascade process where a tube of length l is first broken into two pieces of length $l/2$, which each in turn break into pieces of length $l/4$, we conclude that

$$\gamma_T(l/2) = \sum_{k=2}^{\infty} \gamma_k(l). \tag{S6}$$

More generally, we conclude that

$$\gamma_T(l/2^m) = \sum_{k=m+1}^{\infty} \gamma_k(l). \tag{S7}$$

From this one obtains

$$\gamma_m(l) = \gamma_T(l/2^{m-1}) - \gamma_T(l/2^m) \tag{S8}$$

for all $m \geq 1$. Using Eqs. (S3) and (S4) this yields

$$p_m(l) = \frac{V_f(l/2^{m-1}) - V_f(l/2^m)}{V_f(l)}. \tag{S9}$$

Note that the Eqs. (9) and (10) of the main text ensure that the probabilities given by Eq. (S9) are well-behaved, convergent, and satisfy Eq. (S2). Substituting Eq. (S9) into Eq. (S1) yields Eq. (8) of the main text.

4 Solutions to the differential equation for the full cascade model

For convenience, using Eqs. (S4), (S8), and (S9), Eq. (S1) can be written as

$$\frac{dc(l,t)}{dt} = -\gamma_T(l) c(l,t) + \sum_{m=1}^{\infty} 2^{2m} \gamma_m(2^m l) c(2^m l, t). \tag{S10}$$

Since this equation is linear in the $c(l,t)$ and since it describes a cascading process in which tubes are broken into 2^m fragments of equal length, the solution must have the form

$$c(l,t) = \sum_{n=0}^{\infty} f_n(l,t) c(2^n l, 0) \tag{S11}$$

where $c(l,0)$ is the value of $c(l,t)$ at $t=0$. Since this equation must hold for all choices of $c(l,0)$, setting $t=0$ yields

$$f_n(l,0) = \begin{cases} 1 & \text{if } n=0 \\ 0 & \text{if } n>0 \end{cases} . \tag{S12}$$

Substituting Eq. (S11) into Eq. (S10), and rearranging the sum by diagonals, yields

$$\begin{aligned} &\sum_{k=0}^{\infty} \frac{df_k(l,t)}{dt} c(2^k l, 0) \\ &\quad = -\gamma_T(l) \sum_{k=0}^{\infty} f_k(l,t) c(2^k l, 0) \\ &\qquad + \sum_{k=1}^{\infty} \sum_{m=1}^{k} 2^{2m} \gamma_m(2^m l) f_{k-m}(2^m l, t) c(2^k l, 0). \end{aligned} \tag{S13}$$

By setting $c(2^k l, 0) = 0$ for $k > 0$, this equation yields

$$\frac{df_0(l,t)}{dt} = -\gamma_T(l) f_0(l,t). \tag{S14}$$

By setting $c(2^k l, 0) = 0$ for all k except $k = n$ where $n \geq 1$ yields

$$\frac{df_n(l,t)}{dt} = -\gamma_T(l) f_n(l,t) + \sum_{m=1}^{n} 2^{2m} \gamma_m(2^m l) f_{n-m}(2^m l, t). \tag{S15}$$

Equation (S14), with the initial condition given in Eq. (S12), is easily integrated to yield

$$f_0(l,t) = e^{-\gamma_T(l) t}. \tag{S16}$$

Equation (S15) with the initial condition given in Eq. (S12) can be formally integrated to yield, for $n > 0$,

$$f_n(l,t) = \int_0^t e^{-\gamma_T(l)(t-t')} \sum_{m=1}^{n} 2^{2m} \gamma_m(2^m l) f_{n-m}(2^m l, t') dt'. \tag{S17}$$

Since $n - m$ is always less than n, this equation can be used to obtain $f_n(l,t)$ for successively higher n. For example, for $n = 1$ this equation becomes

$$f_1(l,t) = \int_0^t e^{-\gamma_T(l)(t-t')} 2^2 \gamma_1(2l) f_0(2l, t') dt'. \tag{S18}$$

Substituting Eq. (S16) into this equation and performing the integration yields

$$f_1(l,t) = 2^2 \gamma_1(l) \frac{e^{-\gamma_T(2l)t} - e^{-\gamma_T(l)t}}{\gamma_T(l) - \gamma_T(2l)}. \tag{S19}$$

Due to the sum appearing in Eq. (S17), the number of terms in $f_n(l,t)$ grows exponentially with n. Generally $c(l,0)$ will fall off rapidly with l for sufficiently large l. Hence, the sum in Eq. (S11) can be cut off for sufficiently large n. Still, this n can be large. For the data analysis reported here, the smallest bin size used was $\Delta l = 1/2^5$ μm and the tube lengths spanned 0 to 2^5 μm. The largest n used in this analysis was 10. The number of terms in the

analytic expression for $f_{10}(l,t)$ is 2^9; since the number of terms grows exponentially as a function of n, computer assisted mathematics can be used to generate terms. We determined the terms diagrammatically by the method described below.

The diagrammatic method is based on the observation that each term, in the analytic expression for $f_n(l,t)$, corresponds to a particular cascade by which tubes of length l at time t are produced by the fragmentation of tubes initially of length $2^n l$ through successive encounters with bubbles. As a first step toward generating the terms of $f_n(l,t)$, it is useful to construct a list of all possible cascades by which a tube of length l can be generated from a tube of length $2^n l$. For the given n, there are are up to $n-1$ cascade steps, this maximum number corresponding to the case where the tube of length l results from a cascade in which two fragments were produced with each encounter of a bubble by the $n-1$ successive ancestors of the tube. To generate the complete list of possible cascades for the given n it is useful to generate the list of $n+1$ digit binary numbers whose binary sequence begins with 1 and ends with 1. An example of such a list is given here for the case $n=4$.

4	3	2	1	0	
t_4	t_3	t_2	t_1	t	
$2^4 l$	$2^3 l$	$2^2 l$	$2l$	l	
1	0	0	0	1	$4 \to 0$
1	0	0	1	1	$4 \to 1 \to 0$
1	0	1	0	1	$4 \to 2 \to 0$
1	0	1	1	1	$4 \to 2 \to 1 \to 0$
1	1	0	0	1	$4 \to 3 \to 0$
1	1	0	1	1	$4 \to 3 \to 1 \to 0$
1	1	1	0	1	$4 \to 3 \to 2 \to 0$
1	1	1	1	1	$4 \to 3 \to 2 \to 1 \to 0$

(S20)

Above this list of numbers, we associate a number, time, and length with each column of digits to facilitate the construction of the terms of $f_n(l,t)$ Shown to the right of the list of binary numbers is the cascade associated with each number. The zeros in the binary numbers are interpreted as steps that are skipped in the corresponding cascade. For example, the first entry in the list, 10001, corresponds to a cascade where a tube of length l was produced directly from a tube of length $2^4 l$ that was fragmented into 2^4 tubes through one encounter with a bursting bubble. The second entry in the list, 10011, corresponds to the case where a tube of length $2^4 l$ was first fragmented into 2^3 tubes of length $2l$ by an encounter with a bursting bubble. Some of these tubes in turn were broken in two to produce tubes of length l through an encounter with another bursting bubble. As a final example, the entry 11111 corresponds to the cascade in which tubes of length $2^4 l$ were broken in two to produce tubes of length $2^3 l$ through an encounter with a bursting bubble. In turn, some of these tubes were broken in two to produce tubes of length $2^2 l$ through the encounter with another bursting bubble. In turn, some of these tubes were broken in two to produce tubes of length $2l$ through an encounter with another bursting bubble. In turn, some of these tubes were broken in two to produce tubes of length l through the encounter with another bursting bubble. These tables can be used to write down the series of nested integrals that constitute a given term of $f_n(l,t)$.

The term corresponding to an entry of a table of cascades, such as that of Eq. (S20), for $f_n(l,t)$ is constructed as follows. The leftmost bit (a 1) has associated with it the time t_n and the length $2^n l$. We also associate with it the function

$$e^{-\gamma_T (2^n l) t_n}. \tag{S21}$$

Suppose the next bit to the right that is nonzero has associated with it the integer r, time t_r, and the length $2^r l$. With the n to r transition we associate the integral operator

$$2^{2(n-r)} \gamma_{n-r}(2^n l) \int_0^{t_r} dt_n e^{-\gamma_T (2^r l)(t_r - t_n)} \tag{S22}$$

that operates on the function Eq. (S21). Thus, with the 1 bit at r we associate the function that results when this operator operates on the function Eq. (S21):

$$2^{2(n-r)} \gamma_{n-r}(2^n l) \int_0^{t_r} dt_n e^{-\gamma_T (2^r l)(t_r - t_n)} e^{-\gamma_T (2^n l) t_n}. \tag{S23}$$

Suppose the next 1 bit to the right is at the position associated with the integer s, the time t_s, the tube length $2^s l$. With the r to s transition we associate the operator

$$2^{2(r-s)}\gamma_{r-s}(2^r l)\int_0^{t_s} dt_r e^{-\gamma_T(2^s l)(t_s-t_r)} \tag{S24}$$

which has the same form as Eq. (S22). This operator operates on the function Eq. (S23) associated with the 1 bit at position r. Thus, we associate with the 1 bit at position s the function

$$\begin{aligned} &2^{2(r-s)}2^{2(n-r)}\gamma_{r-s}(2^r l)\gamma_{n-r}(2^n l) \\ &\quad\times\int_0^{t_s} dt_r e^{-\gamma_T(2^s l)(t_s-t_r)} \\ &\qquad\times\int_0^{t_r} dt_n e^{-\gamma_T(2^r l)(t_r-t_n)}e^{-\gamma_T(2^n l)t_n}. \end{aligned} \tag{S25}$$

This process is iterated. With the right most 1 bit we have associated the integer 0, the time $t = t_0$ and the length l. Let the first 1 bit to the left of this bit have associated with it the integer u, the time t_u, and the tube length $2^u l$. Applying the operator for the u to 0 transition, which also has the form Eq. (S24), to the function associated with the 1 bit at position u one obtains

$$\begin{aligned} &2^{2u}\cdots 2^{2(r-s)}2^{2(n-r)}\gamma_u(2^u l)\cdots\gamma_{r-s}(2^r l)\gamma_{n-r}(2^n l) \\ &\quad\times\int_0^{t} dt_u e^{-\gamma_T(2^s l)(t-t_u)}\cdots \\ &\qquad\times\int_0^{t_s} dt_r e^{-\gamma_T(2^s l)(t_s-t_r)} \\ &\qquad\quad\times\int_0^{t_r} dt_n e^{-\gamma_T(2^r l)(t_r-t_n)}e^{-\gamma_T(2^n l)t_n}. \end{aligned} \tag{S26}$$

This is the full term of $f_n(l,t)$ associated with the cascade

$$2^n l \to 2^r l \to 2^s l \to \cdots 2^u l \to l. \tag{S27}$$

Inverting the order of the powers of 2 appearing at the left of Eq. (S26) one sees that

$$2^{2(n-r)}2^{2(r-s)}\cdots 2^{2(v-u)}2^{2u} = 2^{2n}. \tag{S28}$$

Hence Eq. (S26) simplifies to

$$\begin{aligned} &2^{2n}\gamma_u(2^u l)\cdots\gamma_{r-s}(2^r l)\gamma_{n-r}(2^n l) \\ &\quad\times\int_0^{t} dt_u e^{-\gamma_T(2^s l)(t-t_u)}\cdots \\ &\qquad\times\int_0^{t_s} dt_r e^{-\gamma_T(2^s l)(t_s-t_r)} \\ &\qquad\quad\int_0^{t_r} dt_n e^{-\gamma_T(2^r l)(t_r-t_n)}e^{-\gamma_T(2^n l)t_n}. \end{aligned} \tag{S29}$$

The integrations can be carried out. The general form is given by

$$\begin{aligned} &\int_0^{t_0} dt_1 e^{-\gamma_0(t_0-t_1)}\int_0^{t_1} dt_2 e^{-\gamma_1(t_1-t_2)}\cdots \\ &\qquad\times\int_0^{t_{n-1}} dt_n e^{-\gamma_{n-1}(t_{n-1}-t_n)}e^{-\gamma_n t_n} \\ &= (-1)^n\sum_{m=0}^{n}\frac{e^{-\gamma_m t_0}}{\prod_{i=0;i\neq m}^{n}(\gamma_m-\gamma_i)} \end{aligned} \tag{S30}$$

For example, one has

$$\begin{aligned}&\int_0^{t_0} dt_1 e^{-\gamma_0(t_0-t_1)}e^{-\gamma_1 t_1}\\&= -\frac{e^{-\gamma_1 t_0}}{\gamma_1-\gamma_0} - \frac{e^{-\gamma_0 t_0}}{\gamma_0-\gamma_1},\end{aligned} \tag{S31}$$

$$\begin{aligned}&\int_0^{t_0} dt_1 e^{-\gamma_0(t_0-t_1)} \int_0^{t_1} dt_2 e^{-\gamma_1(t_1-t_2)}e^{-\gamma_2 t_2}\\&= \frac{e^{-\gamma_2 t_0}}{(\gamma_2-\gamma_0)(\gamma_2-\gamma_1)}\\&\quad + \frac{e^{-\gamma_1 t_0}}{(\gamma_1-\gamma_0)(\gamma_1-\gamma_2)}\\&\quad + \frac{e^{-\gamma_0 t_0}}{(\gamma_0-\gamma_1)(\gamma_0-\gamma_2)},\end{aligned} \tag{S32}$$

and

$$\begin{aligned}&\int_0^{t_0} dt_1 e^{-\gamma_0(t_0-t_1)} \int_0^{t_1} dt_2 e^{-\gamma_1(t_1-t_2)}\\&\qquad \times \int_0^{t_2} dt_3 e^{-\gamma_2(t_2-t_3)}e^{-\gamma_3 t_3}\\&= -\frac{e^{-\gamma_3 t_0}}{(\gamma_3-\gamma_0)(\gamma_3-\gamma_1)(\gamma_3-\gamma_2)}\\&\quad - \frac{e^{-\gamma_2 t_0}}{(\gamma_0-\gamma_2)(\gamma_1-\gamma_2)(\gamma_2-\gamma_3)}\\&\quad - \frac{e^{-\gamma_1 t_0}}{(\gamma_1-\gamma_0)(\gamma_1-\gamma_2)(\gamma_1-\gamma_3)}\\&\quad - \frac{e^{-\gamma_0 t_0}}{(\gamma_0-\gamma_1)(\gamma_0-\gamma_2)(\gamma_0-\gamma_3)}.\end{aligned} \tag{S33}$$

As an illustrative example, we use the diagrammatic technique to construct $f_2(l,t)$. In this case $n=2$ and the list of all possible cascades is

$$\begin{array}{ccccll} 2 & 1 & 0 & & \\ t_2 & t_1 & t_0 & & \\ 2^2 l & 2l & l & & \\ 1 & 0 & 1 & 2\to 0 & T_{21} \\ 1 & 1 & 1 & 2\to 1\to 0 & T_{22} \end{array} \tag{S34}$$

where T_{21} and T_{22} are the names we have given to the terms of $f_2(l,t)$ for the two possible cascades. The diagrammatic techniques yield

$$T_{21} = 2^4\gamma_2(2^2 l)\int_0^{t_0} dt_2 e^{-\gamma_T(l)(t_0-t_2)}e^{-\gamma_T(2^2 l)t_2} \tag{S35}$$

and

$$\begin{aligned}&T_{22}(t_0)\\&\quad = 2^4\gamma_1(2l)\gamma_1(2^2 l)\\&\qquad \times \int_0^{t_0} dt_1 e^{-\gamma_T(l)(t_0-t_1)}\\&\qquad\quad \times \int_0^{t_1} dt_2 e^{-\gamma_T(2l)(t_1-t_2)}e^{-\gamma_T(2^2 l)t_2}.\end{aligned} \tag{S36}$$

Carrying out the integrations yield

$$T_{21}(t_0) = -16\gamma_2(4l)\left(\frac{e^{-\gamma_T(4l)t_0}}{\gamma_T(4l)-\gamma_T(l)} + \frac{e^{-\gamma_T(l)t_0}}{\gamma_T(l)-\gamma_T(4l)}\right). \tag{S37}$$

and

$$\begin{aligned} &T_{22}(t_0) \\ &\quad = 16\gamma_1(2l)\gamma_1(4l) \\ &\qquad \times\left(\frac{e^{-\gamma_T(4l)t_0}}{[\gamma_T(4l)-\gamma_T(l)][\gamma_T(4l)-\gamma_T(2l)]}\right. \\ &\qquad\quad + \frac{e^{-\gamma_T(2l)t_0}}{[\gamma_T(2l)-\gamma_T(l)][\gamma_T(2l)-\gamma_T(4l)]} \\ &\qquad\quad \left. + \frac{e^{-\gamma_T(l)t_0}}{[\gamma_T(l)-\gamma_T(2l)][\gamma_T(l)-\gamma_T(4l)]}\right). \end{aligned} \tag{S38}$$

Setting $t_0 = t$, one has

$$f_2(l,t) = T_{21}(t) + T_{22}(t). \tag{S39}$$

5 Single bifurcation model

The single bifurcation model, which uses Eq. (7) instead of Eq. (6) in combination with Eqs. (2)-(5) of the main text, is also exactly solvable using the methods outline above. The solution is somewhat simpler because only fragmentation cascades in which the tubes are broken in two at each cascade step are allowed. Using main text Eqs. (4), (5), (7) and SI Eq. (S4), main text Eq. (2) yields

$$\frac{dc(l,t)}{dt} = -\gamma_T(l)c(l,t) + 4\gamma_T(2l)c(2l,t). \tag{S40}$$

Substituting Eq. (S11) into this equation yields

$$\frac{df_0(l,t)}{dt} = -\gamma_T(l)f_0(l,t) \tag{S41}$$

and, for $n > 0$,

$$\frac{df_n(l,t)}{dt} = -\gamma_T(l)f_n(l,t) + 4\gamma_T(2l)f_{n-1}(l,t), \tag{S42}$$

where the boundary conditions Eq. (S12) still apply. Using the boundary conditions these two equations can be integrated to yield

$$f_0(l,t) = e^{-\gamma_T(l)t} \tag{S43}$$

and

$$f_n(l,t) = 4\gamma_T(2l)\int_0^t e^{-\gamma_T(l)(t-t')}f_{n-1}(2l,t')dt'. \tag{S44}$$

It is now evident that the $f_n(l,t)$ can be generated from the $f_{n-1}(l,t)$ through repeated substitution, beginning with the substitution of Eq. (S43) into Eq. (S44) for $n = 1$. $f_n(l,t)$ has the same form as the term corresponding to the $111\cdots1$ cascades of the model discussed in SI section 4 above, except the factor $\gamma_1(2l)\gamma_1(2^2l)\cdots\gamma_1(2^n)$ appearing in this term is replaced by factor $\gamma_T(2l)\gamma_T(2^2l)\cdots\gamma_T(2^n)$, see for example Eq. (S38).

6 Numerical procedures

6.1 Constructing the experimental concentration distributions

The fluorescent microscope technique, used to construct the concentration distribution $c(l,t)$ of tube lengths at various time points, produces a list of tube lengths at these time points. To produce an experimentally determined $c(l,t)$, the number of tubes n_i whose lengths l fell within each of the bin intervals $l_i < l <= l_i + \Delta l$, were counted, where Δl is the bin width which was taken to be $\Delta l = 1/32$ μm. The resulting unnormalized

concentration distribution consisted of the list of n_i as a function of the successive bin locations l_i, where $l_{i+1} = l_i + \Delta l$ and $l_0 = 0$. Since Eq. (11) of the main text is nonlinear in $c(l,t)$, the numerical concentration must be normalized. To determine the normalization constant the tube length per unit volume was calculated from the known concentration of the oligomers forming the tubes under the assumption that all the oligomers resided within the tubes. Total tube length is defined as

$$l_T = \int_0^\infty l c(l,t) dl. \tag{S45}$$

The normalization constant a that converts the n_i into the normalized concentration distribution $c_i = a n_i$ was determined by requiring

$$\sum_i (l_i + \Delta l/2) c_i \Delta l = l_T. \tag{S46}$$

The tube length per unit volume l_T was computed via

$$l_T = \frac{N_0 b_s n_f c_s}{d_f}. \tag{S47}$$

where N_0 is the Avogadro constant, $b_s = 0.34$ nm is the spacing between successive base pairs in duplex DNA, $n_f = 10.5$ also happens to be the number of base pairs for one full turn of duplex DNA (measured in base-pair stacking units, b_s) of the DNA nanotube when a complete ring of tiles is added to a tube end, $c_s = 3.5$ μM is the concentration of a given tile in the stock solution, and $d_f = 20$ is the factor by which the concentration of the stock solution is diluted in preparing the sample solution. For our system $l_T = 3.76 \times 10^{14}$ μm/L.

6.2 Averaging over a bin width

The numerically obtained c_i should be regarded as $c(l,t)$ averaged over the intererval $l_i < l <= l_i + \Delta l$; that is,

$$c_i(t) = \frac{1}{\Delta l} \int_{l_i}^{l_i + \Delta l} c(l,t) dl. \tag{S48}$$

This matters particularly when the experimentally determined $c_i(0)$ is used as the initial concentration distribution in Eq. (S11) to calculate the model $c_i(t)$. When using binned data, one must average Eq. (S11) over a bin width such that

$$\langle c(l,t) \rangle_{l_i} = \sum_{n=0}^{\infty} \langle f_n(l,t) c(2^n l, 0) \rangle_{l_i} \tag{S49}$$

where the $\langle F(i) \rangle$ of a function F is defined as

$$\langle F(l) \rangle_{l_i} = \frac{1}{\Delta l} \int_{l_i}^{l_i + \Delta l} F(l) dl. \tag{S50}$$

We note that even though Δl may be small, $c(2^n l, 0)$ can be strongly varying over this interval when n is large. Similarly, $f_n(l,t)$ can also be strongly varying over this interval when n is large because it contains quantities that depend on $2^n l$. For this reason the value of $f_n((l_i + \Delta l/2), t) c(2^n (l_i + \Delta l/2), 0)$ may not be a good approximation of $\langle f_n(l,t) c(2^n l, 0) \rangle_{l_i}$, necessitating the averaging. In computing the term $\langle f_n(l,t) c(2^n l, 0) \rangle_{l_i}$ by numerical summation the integration a step size of $\Delta l / 2^n$ was employed.

6.3 End joining

For the case when end joining is included, a numerical integration procedure was used in which the $\langle c(l,t) \rangle_{l_i}$ at time $t = t_{j+1}$ are computed for the $\langle c(l,t) \rangle_{l_i}$ at time $t = t_j$ via the following update algorithm

$$\begin{aligned} \langle c(l, t_{j+1}) \rangle_{l_i} &= \sum_{n=0} \langle f_n(l, t_{j+1} - t_j) \langle c(2^n l, t_i) \rangle_l \rangle_{l_i} \\ &\quad + E_J(l_i, t_j)(t_{i+1} - t_i) \end{aligned} \tag{S51}$$

where $E_J(l_i, t_j)$ is

$$\begin{aligned} E_J(l,t) &= -\int_0^\infty dl' k(l,l') c(l,t) c(l',t) \\ &\quad + \int_0^l dl' k(l', l-l') c(l',t) c(l-l',t) \end{aligned} \tag{S52}$$

numerically evaluated for $l = l_i$ at $t = t_j$ using the $\langle c(l, t_j)\rangle_{l_i}$ for the $c(l,t)$.

6.4 Search algorithm

The unknown to be extracted from the data is the fragmentation volume function $V_f(l)$. A search algorithm was implemented that, under the constraints that $V_f(0) = 0$ and that $V_f(l)$ be a monotonically increasing function of l, sought to find a continuous piecewise linear function $V_f(l)$ that produced the best fit between the data and the numerical model. The function is specified by the values V_i of $V_f(l)$ at the tube length values l_i where the slope of $V_f(l)$ can change. The l_i were chosen according to:

$$\begin{aligned} l_0 &= 0, \\ l_1 &= 1/32, \\ l_2 &= 3/32, \\ l_3 &= 7/32, \\ l_4 &= 15/32 \\ l_i &= i - 4 - 1/32 \text{ for } i > 4. \end{aligned} \tag{S53}$$

where the tube lengths l_i are in microns. The nonuniform distribution of the l_i for $i < 5$ was chosen to allow the investigation of $V_f(l)$ at the length scale of the smallest tube fragments observed. The initial V_i were chosen to be

$$V_i = 0.01875i \tag{S54}$$

where the fragmentation volumes $V_i = V(l_i)$ are the fragmentation volumes in microliters (μl). The values of $V(l)$ for l not equal to one of the l_i were determined by linear interpolation between the l_i and l_{i+1} for which $l_i < l < l_{i+1}$.

The search algorithm proceeded by stochastically modifying the function $V_f(l)$ to produce the new function $V_f^{new}(l)$. The goodness of the fit of the model using $V_f^{new}(l)$ as the fragmentation volume was determined and compared with that of $V_f(l)$. If the fit using $V_f^{new}(l)$ was as good or better than that for $V_f(l)$, then V_f^{new} became the new $V_f(l)$. Otherwise $V_f^{new}(l)$ was discarded and $V_f(l)$ was retained as the fragmentation volume function. Each iteration of this process was counted as a generation. Good convergence of $V_f(l)$ to the optimum was obtained in 10,000 generations.

The procedure by which V_f^{new} is created is the following: An integer i_a with a uniform distribution on the interval $1 \le i_a \le 35$ was produced by a random number generator. A second random integer i_b with a uniform distribution on the interval $0 \le i_b \le 7$ was produced by a second random number generator. From these two random integers, two new random integers were created

$$\begin{aligned} i_1 &= i_a - i_b \\ i_2 &= i_a + i_b \end{aligned} \tag{S55}$$

If i_1 was less than 1 it was reset to 1. If i_2 was greater than 35 it was reset to 35. Next, two random numbers r_1 and r_2 were generated from a random number generator which produced a uniform distribution between 0 and 1. If $i_2 < 35$ the $V_f^{new}(l_i)$ was created from $V_f(l_i)$ according to

$$\begin{aligned} V_f^{new}(l_i) &= V_f(l_i) + [V_f(l_{i_1-1}) - V_f(l_{i_1}))]r_1 \\ &\quad + [V_f(l_{i_2+1}) - V_f(l_{i_2})]r_2 \end{aligned} \tag{S56}$$

for $l_{i_1} \le l_i \le l_{i_2}$ and

$$V_f^{new}(l_i) = V_f(l_i) \tag{S57}$$

otherwise. If $i_2 = 35$ the $V_f^{new}(l_i)$ was created from $V_f(l_i)$ according to

$$V_f(l_i)^{new}(l) = V_f(l_i) + [V_f(l_{i_1-1}) - V_f(l_{i_1}))]r_1 + r_2 \tag{S58}$$

for $l_{i_1} \leq l_i$ and

$$V_f^{new}(l_i) = V_f(l_i) \tag{S59}$$

otherwise. This procedure randomly shifts a block, of variable width and position, of the function $V_f(l)$ up or down restricted to the maximum range allowed consistent with maintaining monotonicity. This procedure was adopted because the search algorithm was less susceptible to hang up at local optima than a procedure in which the $V_f(l_i)$ were individually updated.

In order to compare the model with the experiment, both the $c(l,t)$ measured experimentally and computed via the model were averaged over 1 μm intervals for successive intervals $l_i <= l < l_i + 1$ μm, where $l_{i+1} = l_i + 1$ starting with $l_0 = 0$. Let $\bar{c}(l_i, t_j)$ denote the experimental length distribution averaged over the ith interval and let $\bar{c}_m(l_i, t_j)$ denote the corresponding quantity calculated by the model. The quantity SD_1, consisting of the squared difference between $\bar{c}(l_i, t_j)$ and $\bar{c}_m(l_i, t_j)$ summed over all intervals i and and time points t_j at which the tube length distributions were measured, was used to compare the data with the model:

$$SD_1 = \sum_j \sum_i [\bar{c}(l_i, t_j) - \bar{c}_m(l_i, t_j)]^2. \tag{S60}$$

In addition, to assess the effectiveness of bursting bubbles in breaking short tubes the following averages were computed both for the experimental data and for the model

$$\bar{b}(\Delta_i, t_j) = \frac{1}{\Delta_i} \int_0^{\Delta_i} c(l, t_j) dl, \tag{S61}$$

where

$$\Delta_i = \frac{\Delta l}{2^i}. \tag{S62}$$

and $\Delta l = 1$ μm. That is, averages over the intervals with one end at the origin $l = 0$, were computed for 1/2, 1/4, 1/8, and 1/16 micron intervals. Let $\bar{b}(\Delta_i, t_j)$ denote these quantities computed for the experimental data and let $\bar{b}_m(\Delta_i, t_j)$ denote the corresponding quantities computed by the model. Then, the quantity SD_2, given by

$$SD_2 = \sum_j \sum_{i=1}^{4} [\bar{b}(\Delta_i, t_j) - \bar{b}_m(\Delta_i, t_j)]^2, \tag{S63}$$

was used to compare the data with the model for short tubes. The search algorithm sought to minimize the combined quantity

$$SD = SD_1 + W \cdot SD_2. \tag{S64}$$

where the weight W was taken to be 5×10^{-4}.

The statistical uncertainty in the determination of V_f, indicated in Fig. 5 was determined by generating new tube length lists from the experimentally obtained tube length lists via resampling using the withdraw from sample with replacement procedure (i.e. bootstrapping). These new tube length lists were binned to produce new $\bar{c}(l_i, t_j)$ distributions that were then processed using the procedures described above to extract the fragmentation volume functions for the resampled data. The mean, variance, and root-mean-square deviation (σ) of the bootstrapped ensemble of resulting fragmentation volumes were then computed. The "standard error of the mean" (S.E.M.) for the V_f parameter estimation is denoted by σ, as plotted in Fig. 5.

7 Derivation of the end-to-end joining rate constant

Here we derive Eq. (13) of the main text, the rate constant for the end-joining of two of our DNA nanotubes. For diffusion-controlled reactions, the rate constant for a second order reaction in which reactant 1 and reactant 2 are joined has the form

$$k_{12} = 4\pi(D_1 + D_2)L_{12} \tag{S65}$$

where D_1 and D_2 are the diffusion constants for reactant 1 and 2, respectively, and L_{12} is a characteristic distance that the reactants must approach each other in order to react [3].

In the present case the reactants are long rods whose reactive sites are at the ends of the rods. In this case both translational and rotational diffusion can be expected to play a role. However, in dilute solutions where the mean distance between the reactants is much larger than the length of the rods, translational diffusion will set the time scale on which the reactants find each other. Hence, D_1 and D_2 will be taken to be the translational diffusion constants for the rods. The diffusion constant D can be obtained from the rod mobility μ via the Einstein relation

$$D = \mu k_B T \tag{S66}$$

where k_B is Boltzmann's constant and T is the absolute temperature. Our rods are long compared to their radius ($R = 4$ nm). Hence, we have $R/l \ll 1$, where l is the rod length. To leading order in R/l, the mobility of a rod translated parallel to its long axis is (Ref. [4])

$$\mu_{||} = \frac{\ln(l/R)}{2\pi\eta l}, \tag{S67}$$

where η is the dynamic viscosity of the liquid. The mobility of the rod in a direction perpendicular to the long axis is half that of $\mu_{||}$:

$$\mu_T = \frac{1}{2}\mu_{||}. \tag{S68}$$

There are three independent directions of motion: one parallel, and two perpendicular to the long axis of the rod. Assuming that the orientation distribution of the rod is uniform due to rotational diffusion, the average mobility will be

$$\mu = \frac{2}{3}\mu_{||}. \tag{S69}$$

Hence, the translational diffusion constant for the rod is given by

$$D = \frac{k_B T \ln(l/R)}{3\pi\eta l}. \tag{S70}$$

Eq. (S65) can be written as

$$k_{12} = \frac{4k_B T L_{12}}{3\eta R}\left(\frac{\ln(l_1/R)}{(l_1/R)} + \frac{\ln(l_2/R)}{(l_2/R)}\right). \tag{S71}$$

To determine the reaction's characteristic distance L_{12}, we first note that the DNA nanotubes have a polarity, such that the "+" end of one nanotube can only react with the "-" end of the other nanotube. We further assume that, because the single-stranded sticky ends are flexible, the two nanotubes do not need to be aligned with each other to initiate the joining reaction. Thus, for this purpose we treat the nanotubes as spherical reactants with radii R_1 and R_2, respectively, corresponding to the size of their reactive sites (but still with the diffusion constants D_1 and D_2 derived above). In this case, $L_{12} = R_1 + R_2$. The reactive sites of a rod consist of single-stranded DNA at each end that is able to hybridize with complementary single-stranded DNA on the other rods. These single-stranded DNA domains are 11 bases long (4.7 nm long). Adding this to the 4 nm radius of the rod suggests that the reactive ends can be treated approximately as spheres of radius $R_1 = R_2 = 9$ nm. Consequently, $L_{12} = 18$ nm. The resulting rate constant is likely an overestimate because of the spherical approximation we have made for the geometry of the reactive site and the assumption that a successful reaction occurs every time the reactive sites meet. We therefore introduce an effectiveness parameter $0 < \kappa < 1$. Finally, because both ends of each nanotube can react, we multiply by a factor of two, to arrive at the equation

$$k_{12} = \kappa\frac{12k_B T}{\eta}\left(\frac{\ln(l_1/R)}{(l_1/R)} + \frac{\ln(l_2/R)}{(l_2/R)}\right). \tag{S72}$$

A similar equation for end-to-end joining of rod-like polymers was obtained by Hill [5]. Using our notation, and ignoring constants, his equation can be written as

$$k_{12} \sim \frac{1}{l_1 + l_2}\left(\frac{\ln(l_1)}{l_1} + \frac{\ln(l_2)}{l_2}\right). \tag{S73}$$

The difference between our results can be explained by Hill's assumption that the two rod-like polymers must be approximately aligned with each other in order to react, in contrast to our assumption that reactive ends can initiate successful binding regardless of their initial relative orientation. Again, our result is an overestimate.

Comparison to oligonucleotide hybridization suggests plausible ranges for the fraction of effective collisions, κ. Approximating oligonucleotides of length N nucleotides as spheres of radius $R_1 = R_2 = R_s = \sqrt{N} \times 0.43$ nm, we follow the analysis of Calef and Deutch [3] and use $D_1 = D_2 = D_s = k_B T/6\pi\eta R_s$ and

$$k_{12} = \kappa\ 4\pi(D_1 + D_2)(R_1 + R_2) = \kappa \frac{8k_B T}{3\eta}, \tag{S74}$$

where we have added κ to account for ineffective collisions. Interestingly, this estimate is independent of R_s and thus N; however, we might expect that κ has a dependence upon N. Here we will extract κ from measurements of the rate constant for hybridization of two 10-mers, which was found to be $\sim 1.0 \times 10^7$ /M/s at 30 °C in a 1 M Na^+ buffer [6]. Thus, we have

$$k_{12} = \kappa \times 6.6 \times 10^9 \text{ /M/s} \sim 1.0 \times 10^7 \text{ /M/s} \tag{S75}$$

and thus $\kappa \sim 1.5 \times 10^{-3}$ for 10-mer hybridization, i.e. roughly only 1 in 660 collisions leads to duplex formation. In the case of end-to-end joining of 7-helix DNA nanotubes, each end has 7 length-10 or length-11 sticky ends with distinct sequences (Fig. S1). Presuming that each collision has a 1-in-7 chance of allowing interaction between complementary sticky ends, and presuming that 1 in 660 of such collisions leads to successful end-to-end joining of the nanotubes, we obtain $\kappa_{ref} = 2.2 \times 10^{-4}$. However, because of the slower translational diffusion in nanotubes relative to oligonucleotides, the attempt frequency and success probability could be larger than the estimate provided here, necessitating experimental assessment. In the main text, we note that poorer fits to our experimental data result when larger values of κ are used, providing some evidence in support of our suggested reference value of κ. Here, we also note that even if κ were as large as $122 \times \kappa_{ref}$, the inferred fragmentation volumes remain within a factor of 10 of those reported in Fig. 5.

8 Angular deviation of a rod from the elongation axis due to Brownian motion

Although a rod shaped object subjected to elongation flow is expected to orient along the direction of elongation, Brownian fluctuation however, acts to misalign the rod through rotational diffusion. This diffusion rate is greater for smaller objects and may reduce how effectively elongation flow can shear nanorods. Here we compute the mean-square-angular deviation of the rod axis from the axis of elongation for a rod subjected to pure elongation flow and show that this deviation is equal to the Péclet number for a suitable choice of characteristic velocity and characteristic length.

For the analysis, we consider the case when the tube is much longer than its radius, so that terms need be kept only to leading order in l/R, where l is the tube length and R is the tube radius. We also use the small angle approximation $\sin(\theta) \approx \theta$, where θ is the angle of misalignment of the tube from the axis of elongation. This axis is taken to lie along the z axis. In the main text, we show that our experimental conditions warrant these approximations.

Consider pure elongation flow, with axis of elongation oriented along the z axis, and with stagnation point at the origin. The radial, ϕ and z components of the velocity field are given by

$$\begin{pmatrix} u_r \\ u_\phi \\ u_z \end{pmatrix} = \begin{pmatrix} -\dot{\epsilon} r/2 \\ 0 \\ \dot{\epsilon} z \end{pmatrix}. \tag{S76}$$

The stress on a surface element of the rod along the axis of elongation [7] is given by

$$\sigma_{rz} = \frac{\eta \dot{\epsilon} z}{R \ln(l/2R)}. \tag{S77}$$

If the rod is misaligned from the z axis by a small angle θ, it will experience a restoring torque given by

$$T_r = 4\pi R \int_{-l/2}^{l/2} \sigma_{rz} z \theta dz = \frac{\pi \eta \dot{\epsilon} l^3 \theta}{3 \ln(l/2R)}, \tag{S78}$$

where the rod's center has been chosen to be at the stagnation point.

A torque will also be generated as the rod is rotated in the fluid due to opposing forces generated by the fluid viscosity. This torque is given by

$$T_\eta = \eta_R \frac{d\theta}{dt}, \tag{S79}$$

where the torque constant is given by

$$\eta_R = \frac{\pi \eta l^3}{3\ln(l/R)}. \tag{S80}$$

See for example J. Riseman and J. G. Kirkwood [4], or S. Broersma [8]. Associated with this frictional torque is a fluctuating torque T_n that has zero mean and whose two time correlation function is given by

$$\langle T_n(t) T_n(t') \rangle = 2\eta_R k_B T \delta(t - t'). \tag{S81}$$

This torque induces Brownian motion with a rotatory diffusion constant given by

$$D_r = \frac{k_B T}{\eta_R}. \tag{S82}$$

See for example D. A. Tsyboulski, *et al.* [9].

Torque balance requires

$$T_\eta + T_r = T_n. \tag{S83}$$

Substituting Eqs. (S78) and (S79) into this equation and using approximation $\ln(l/2R) \sim \ln(l/R)$, since we are considering the case when $l \gg R$, reduces this equation to the Langevin equation

$$\frac{d\theta}{dt} + \dot{\epsilon}\theta = \frac{T_n}{\eta_R}. \tag{S84}$$

To determine the mean-square deviation of θ from zero due to Brownian fluctuations, it is convenient to convert this differential equation into the integral equation

$$\theta = \frac{1}{\eta_R} \int_{-\infty}^{t} e^{-\dot{\epsilon}(t-t')} T_n(t') dt. \tag{S85}$$

It is then straightforward to show that

$$\langle \theta^2 \rangle = \frac{k_B T}{\eta_R \dot{\epsilon}} = \frac{3 k_B T \ln(l/R)}{\pi \eta \dot{\epsilon} l^3}. \tag{S86}$$

.

Following M. Manhart [10], we introduce the Péclet number

$$\mathrm{Pe} = \frac{\partial u_z / \partial z}{D_r} = \frac{\dot{\epsilon}}{D_r}. \tag{S87}$$

Using Eqs. (S76) and (S82), and comparing to Eq. (S86) one finds

$$\langle \theta^2 \rangle = \frac{1}{\mathrm{Pe}}. \tag{S88}$$

9 Analysis of the fragmentation of tube-like multilamellar vesicles

Here we estimate the elongation rate that is required to fragment, to 1 μm lengths, the tubular multilamellar vesicles whose fragmentation Zhu and Szostak [11] have studied as a possible means by which protobionts may have carried out cell division.

In a typical experiment, the vesicle starts out as a sphere having a radius of 2 μm. The initial volume of the vesicle is 33.5 $\mu\mathrm{m}^3$ and it initial area is 25.1 $\mu\mathrm{m}^2$. Upon incorporating micelles into the vesicle, the vesicle

increases its area 3.7 fold. Due to the impermeability of the wall, the volume remains fixed. To accommodate the increased area while keeping the volume fixed the vesicle adopts a branched filament configuration where the filaments have a radius r of 0.18 μm and the total length of the filaments is 81 μm. When these filaments are sheared by fluid flow they reform spherical vesicles without spilling their contents into the surrounding medium. It is this latter property that makes the fragmentation of these filaments attractive as a primitive form of cell division.

Although Zhu and Szostak showed that this mechanism operates for vesicles made from a variety of lipids, the one that received the most study was olic acid. This molecule is 2.06 nm long. The bilayer lamella has a thickness that is twice this, namely $t = 4.12$ nm. The cross-sectional area presented by the lamella is thus $A_l = 2\pi rt$ or 4.6×10^{-3} μm^2. To estimate the tensile force required to shear a vesicle with a lamella of this cross-section we will assume that the tensile strength of of an olic acid lamella is the same as that of paraffin wax, since the two consist of linear chains of mostly saturated hydrocarbon. The tensile strength σ_T of paraffin wax is roughly 1 MPa [12]. The tensile force required to shear the vesicle is thus $T = \sigma_t A_l = 4.6$ nN. Using this number, $l = 1$ μm, and $R = r$ in Eq. (1) of the main text one finds $\dot{\epsilon} = 2.5 \times 10^6$ sec^{-1}. This is the elongation rate required to fragment the tube like vesicle into fragments 1 μm long. For a multilamellar vesicle, consisting of n lamellar layers, the elongation rate required for fragmentation becomes $\dot{\epsilon} = 2.5 \times 10^6$ sec$^{-1} \times n$.

10 Supplementary Movie

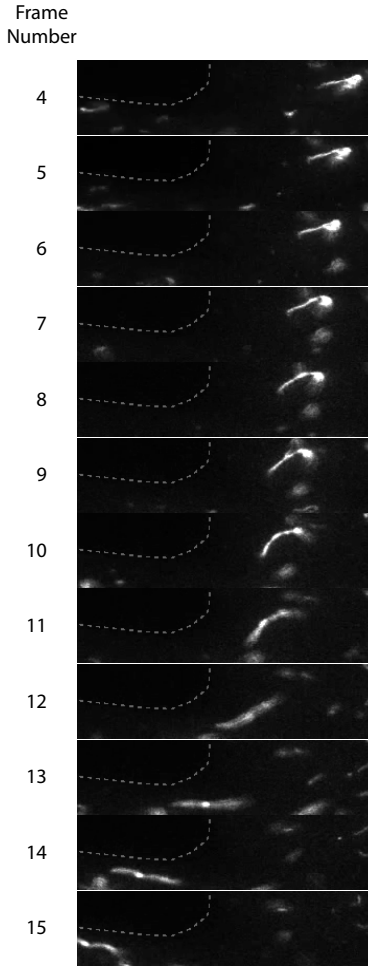

Movie S1. Fluorescence movie (1 frame/sec) of Cy3-labeled DNA nanotubes in a microfluidic channel (dashed lines, height 100 μm) under slow flow rate (right to left, 47 μm/sec in the center). The nanotubes experienced compressional and elongational flows as they enter and exit the side chamber, respectively. The maximum elon-

gational flow in the channel was estimated to be 1.4 /sec, which is, using a conformational relaxation time of 400 ms for the nanotubes, within a factor of two of the critical threshold for polymer stretching [13]. The measured maximum elongational flow during the bursting of a bubble (Fig. S1) is $\sim 10^8$-fold larger than in the channel. Consequently, the elongational flow during the expansion of the bubble hole is expected to orient and stretch DNA nanotubes. Given the longest observed nanotube in the movie is 52 μm, the maximum elongational-flow-induced tension in the channel was calculated to be 1.2 pN (Eq. 1). The maximum generated tension in the movie is more than two-orders of magnitude smaller than the critical tension to break a 7-helix DNA nanotubes (455 pN). The weak hydrodynamic-induced tension is sufficient to explain the absence of nanotube scission in the movie.

References

[1] Yin P, et al. (2008) Programming DNA tube circumferences. *Science* 321:824–826.

[2] Schiffels D, Liedl T, Fygenson DK (2013) Nanoscale structure and microscale stiffness of DNA nanotubes. *ACS nano* 7:6700–6710.

[3] Calef DF, Deutch J (1983) Diffusion-controlled reactions. *Annual Review of Physical Chemistry* 34:493–524.

[4] Riseman J, Kirkwood JG (1950) The intrinsic viscosity, translational and rotatory diffusion constants of rod-like macromolecules in solution. *The Journal of Chemical Physics* 18:512–516.

[5] Hill TL (1983) Length dependence of rate constants for end-to-end association and dissociation of equilibrium linear aggregates. *Biophysical journal* 44:285–288.

[6] Morrison LE, Stols LM (1993) Sensitive fluorescence-based thermodynamic and kinetic measurements of DNA hybridization in solution. *Biochemistry* 32:3095–3104.

[7] Hariadi RF, Yurke B (2010) Elongational-flow-induced scission of DNA nanotubes in laminar flow. *Physical Review E* 82:046307.

[8] Broersma S (1960) Rotational diffusion constant of a cylindrical particle. *The Journal of Chemical Physics* 32:1626–1631.

[9] Tsyboulski DA, Bachilo SM, Kolomeisky AB, Weisman RB (2008) Translational and rotational dynamics of individual single-walled carbon nanotubes in aqueous suspension. *ACS Nano* 2:1770–1776.

[10] Manhart M (2004) Visco-elastic behaviour of suspensions of rigid-rod like particles in turbulent channel flow. *Eur J of Mec B-Fluid* 23:461 – 474.

[11] Zhu TF, Szostak JW (2009) Coupled growth and division of model protocell membranes. *Journal of the American Chemical Society* 131:5705–5713.

[12] DeSain JD, Brady BB, Metzler KM, Curtiss TJ, Albright TV (2009) Tensile tests of paraffin wax for hybrid rocket fuel grains. *AIAA* 5115:1–27.

[13] Smith DE, Chu S (1998) Response of flexible polymers to a sudden elongational flow. *Science* 281:1335–1340.